Projection-based Embedded Discrete Fracture Model (pEDFM) on Corner-point Grid Geometry for Subsurface Flow and Geothermal Modeling

Hosseinimehr, M.; Piguave Tomala, J.P.; Vuik, Cornelis; Hajibeygi, H.

Projection-based Embedded Discrete Fracture Model (pEDFM) on Corner-point Grid Geometry for Subsurface Flow and Geothermal Modeling

Mousa HosseiniMehr[1,a], Janio Paul Piguave Tomala[2,b] ,Cornelis Vuik[1,c], Hadi Hajibeygi[2,d]

[1] Delft Institute of Applied Mathematics, TU Delft, The Netherlands
[2] Department of Geoscience and Engineering, TU Delft, The Netehrlands

[a] S.HosseiniMehr@tudelft.nl; [b] J.P.PiguaveTomala@student.tudelft.nl;
[c] C.Vuik@tudelft.nl; [d] H.Hajibeygi@tudelft.nl

Abstract

We develop projection-based embedded discrete fracture model (pEDFM) on corner-point grids (CPG) for fluid flow and heat transfer in subsurface geological formations. The coupling between the flow and heat transfer is fully-implicit, to allow for stable simulations, specially in presence of highly contrasting fractures. We define independent CPG-based mesh for matrix rock and all 3D fractures, which allows for capturing geologically complex geometries. The connectivities between the non-neighbouring cells are described such that a consistent discrete representation of the embedded fractures are developed within the CPG geometry. Numerical rests are developed first to verify the CPG grid implementation compared with the Cartesian structured ones, and then to illustrate the applicability of the pEDFM for field-scale geologically complex reservoirs.

Significance and Technical Contributions to the Knowledge Base of the Mathematics of Oil Recovery:

- It develops a fully 3D projection-based embedded discrete fracture model (pEDFM).

- It extends pEDFM method for corner-point grid geometry.

Introduction

Geothermal energy offers a lot of opportunities to transfer the energy supply of today to a greener mix (Bertani, 2012; Lund et al., 2011; Burnell et al., 2012, 2015). Safe and efficient development of this low-carbon-based Geo-energy resource depends on accurate and scalable modeling of coupled mass-heat transport in heterogeneous porous media. When it comes to geoscience applications, the main challenges stand as heterogeneity, scales and uncertainty (Moraes et al., 2017; McClure and Horne, 2014).

Simulation models should be able to accurately capture high contrasts in mass and heat heterogeneous properties inside the porous media while providing computational efficiency and maintaining field-scale applicability. Many reservoirs encompass complex geological features (e.g., networks of fractures and faults) with extensive range of conductivities. Such high contrasts influence the flow and heat patterns significantly. Therefore, high fidelity representation of the physical phenomena within the heterogeneous fractured reservoirs is crucial (Berkowitz, 2002). However, there are variety of complex challenges, as the models demand high-resolution grids to be imposed on the entire reservoir (in orders of kilometres) (Praditia et al., 2018). Strong mass-heat coupling and the non-linear behavior of the system results in poor stability and convergence. Multi-phase flow systems (e.g., in high-enthalpy systems) cause more severe issues (Wong et al., 2018). The geo-mechanical processes (i.e., elastic and plastic deformation) (Rossi et al., 2018; Garipov et al., 2016; Gholizadeh Doonechaly et al., 2016a), reactive transport (e.g., geo-chemical interaction between the substances) (Morel and Morgan, 1972; Leal et al., 2017; Salimzadeh and Nick, 2019) and compositional changes (Voskov and Tchelepi, 2012; Voskov, 2017; Cusini et al., 2018) are other among other challenges. The presence of fractures and faults (Gan and Elsworth, 2016; Gholizadeh Doonechaly et al., 2016b; Salimzadeh et al., 2019; Hajibeygi et al., 2011) with wide heterogeneity contrasts significantly increases the computational complexity. These challenges introduce high demands for developing advanced simulation methods that are able to provide efficiency while maintaining accuracy at the desired level (Lie, 2019; Wang et al., 2020; Kozlova et al., 2016).

Geological formations are hardly representable on Cartesian grids, although these simplified gris allow for many conceptual modeling analyses. Realistic formations, however, are more conveniently represented by flexible grids (Lie et al., 2020; Reichenberger et al., 2006). The grid geometry should create a set of discrete cell volumes that approximate the reservoir volume, yet fit the transport process physics, and avoid over complications as much as possible (Ahmed et al., 2015). Unstructured grids allow for many flexibilities, which need to be carefully applied to a computational domain so that the discrete systems do not become over complex (Karimi-Fard et al., 2004; Jiang and Younis, 2016). Without introducing the full flexibility (and at the same time complexity) of the fully unstructured grids, corner-point grid geometries allow for many possibilities in better representation of geological structures. This has made them quite attractive in geoscience industry-grade simulations (Ponting, 1989; Ding et al., 1995; GeoQuest, 2014; Lie, 2019).

Representation of explicit fractures on structured Cartesian grids has been extensively addressed in the literature, starting from the development of embedded discrete modelling approach (Lee et al., 1999; Li and Lee, 2008; Hajibeygi et al., 2011; Lee et al., 2001; Moinfar et al., 2011; Ren et al., 2018). The development of EDFM approach for CPG geometries, however, has not yet been fully addressed. The only existing publication seems to be the one by Xu et al. (2019). The state-of-the-art EDFM formulations have allowed for consistent treatment of fractures, from high to low conductive ranges. This is addressed in projection EDFM (pEDFM) which was originally developed by Tene et al. (2017) for single and multiphase flows. pEDFM quickly was used in many research (Jiang and Younis, 2017; HosseiniMehr et al., 2020a). It is to date yet unknown how the pEDFM formulation and implementation should look like in presence of CPG geometries. The current paper addresses this important development.

In this article, a projection-based embedded discrete fracture model (pEDFM) on corner-point grid (CPG) geometry is presented. Although this fracture model can be used on any flow model, the focus of this article is on simulation of non-isothermal single-phase mass-heat flow in fractured porous

media. Due to the strong non-linearity of the system (mass-heat coupling), two sets of equations (mass and energy balance) are coupled using the fully-implicit (FIM) approach. In the energy balance equation, conduction terms are described for both fluid and rock. To represent realistic and geologically relevant domains, corner-point grid geometry is used. pEDFM is employed in order to explicitly and consistently represent fractures and to provide independent gridding of matrix and fractures regardless of complex geometrical shapes of domains. Here, the applicability of the pEDFM implementation (Tene et al., 2017; HosseiniMehr et al., 2020b) has been extended to a fully generic 3D geometry where it allows for including fractures (or flow barriers) with any orientation on the corner-point grid geometry. This is crucial for practical field-scale applications. In addition to geometrical flexibility of EDFM, the matrix-matrix and fracture-matrix connectivities are re-adjusted to account for projection of fracture plates on the interfaces. This allows for consistent modelling of fractures with generic range of conductivity. The discrete system is obtained for two main unknowns, namely, pressure and temperature on both matrix and fracture network. We assume local thermal equilibrium, meaning that the temperatures in fluid and rock are considered to be equal. This assumption can be recognised as safe for the majority (or perhaps all) of the geo-engineering applications (Coats, 1977) due to large contact area between the liquid and solid phases. Using a number of homogeneous and heterogeneous test cases, the accuracy and applicability of the devised method is demonstrated.

This article is arranged as the following. The governing equations and FIM approach are described in Section 1. The corner-point grid geometry and pEDFM approach is covered in Section 2 and 3. The test cases and their numerical results are shown in Section 4. The paper is concluded in Section 5.

Governing equations

The geothermal system discussed in this article consists of two main governing equations, namely mass and energy conservation law. Assuming local thermal equilibrium, the temperatures of fluid and rock are considered to be identical.

Mass Conservation

The mass balance equation for single-phase fluid flow in porous media with n_{frac} discrete fractures reads

$$\frac{\partial}{\partial t}\left(\phi^m \rho_f\right) - \nabla \cdot \left(\rho_f \frac{1}{\mu_f}\mathbf{K}^m \cdot \nabla p^m\right) = \rho_f q^{mw} + \sum_{i=1}^{n_{\text{frac}}} \rho_f^* \mathcal{Q}^{mf_i}, \quad \text{on} \quad \Omega_m \subseteq \text{Re}^n, \tag{1}$$

for the rock matrix (m) and

$$\frac{\partial}{\partial t}\left(\phi^{f_i} \rho_f\right) - \nabla \cdot \left(\rho_f \frac{1}{\mu_f}\mathbf{K}^{f_i} \cdot \nabla p^{f_i}\right) = \rho_f q^{f_i w} + \rho_f^* \mathcal{Q}^{f_i m} + \sum_{j=1}^{n_{\text{frac}}} \left(\rho_f^* \mathcal{Q}^{f_i f_j}\right)_{j \neq i},$$
$$\text{on} \quad \Omega_{f_i} \subseteq \text{Re}^{n-1} \quad \forall i \in \{1,...,n_{\text{frac}}\}, \tag{2}$$

for the lower dimensional fracture (f_i). The main unknown of this equation is the pressure p. Porosity and permeability of each medium are denoted as ϕ and $\mathbf{K}$. Note that $\mathbf{K}$ is a tensor to account for a generic anisotropic case. Subscripts f and r denote fluid and rock. Superscripts m, f_i and w correspond to matrix, fracture i and well, respectively. ρ and μ are the density and viscosity of the fluid. Additionally, q^{mw} and $q^{f_i w}$ are the source terms (i.e., wells) on matrix m and fracture f_i. Moreover, $\mathcal{Q}^{mf_i}$ and $\mathcal{Q}^{f_i m}$ are the so-called flux exchanges between matrix m and overlapping fracture f_i corresponding to the grid cells where overlap occurs. $\mathcal{Q}^{f_i f_j}$ is the flux exchange from j-th fracture to the i-th fracture on the intersecting elements. Mass conservation always holds, i.e., $\iiint_V \mathcal{Q}^{mf_i}dV = -\iint_{A_{f_i}} \mathcal{Q}^{f_i m}dA$, and

$$\iint_{A_{f_i}} \mathscr{Q}^{f_i f_j} dA = - \iint_{A_{f_j}} \mathscr{Q}^{f_j f_i} dA.$$

The Peaceman well model is used to obtain the flux between the wells and the reservoir:

$$q^{mw} = \frac{PI \cdot \lambda^* \cdot (p^w - p^m)}{\Delta V} \tag{3}$$

and fractures

$$q^{f_i w} = \frac{PI \cdot \lambda^* \cdot (p^w - p^{f_i})}{\Delta A}. \tag{4}$$

Here, PI denotes well productivity index and λ^* is the effective mobility ($\lambda = K/\mu$) between the well and the penetrated grid cells in the medium. ΔV and ΔA are the control volume and control area used in the discrete system for matrix m and fracture f_i respectively. The flux exchange terms $\mathscr{Q}^{mf_i}$, $\mathscr{Q}^{f_i m}$ (matrix-fracture) and $\mathscr{Q}^{f_i f_j}$ (fracture-fracture) are given as:

$$\mathscr{Q}^{mf_i} = CI^{mf_i} \cdot \lambda^* \cdot (p^{f_i} - p^m) \tag{5}$$

$$\mathscr{Q}^{mf_i} = CI^{f_i m} \cdot \lambda^* \cdot (p^m - p^{f_i}) \tag{6}$$

$$\mathscr{Q}^{f_i f_j} = CI^{f_i f_j} \cdot \lambda^* \cdot (p^{f_j} - p^{f_i}), \tag{7}$$

where CI is the connectivity index between each two non-neighboring elements. For instance, the connectivity index between i-th matrix element and j-th fracture element is calculated as $CI_{ij} = \frac{A_{ij}}{\langle d \rangle_{ij}}$. Here, A_{ij} is the area fraction of fracture cell j overlapping with matrix cell i and $\langle d \rangle_{ij}$ is the average distance between these cells.

Energy Balance

Assuming local equilibrium, energy balance on the entire domain reads

$$\frac{\partial}{\partial t}\left((\rho U)^m_{eff}\right) - \nabla \cdot \left(\rho_f H^m_f \frac{1}{\mu_f} \mathbf{K}^m \cdot \nabla p^m\right) - \nabla \cdot \left(\Lambda^m_{eff} \cdot \nabla T^m\right) =$$
$$= \rho_f H^m_f q^{mw} + \sum_{i=1}^{n_{frac}} \rho_f^* H_f^* \mathscr{Q}^{mf_i} + \sum_{i=1}^{n_{frac}} \mathscr{R}^{mf_i},$$
$$\text{on} \quad \Omega_m \subseteq \text{Re}^n, \tag{8}$$

for the rock matrix (m) and

$$\frac{\partial}{\partial t}\left((\rho U)^{f_i}_{eff}\right) - \nabla \cdot \left(\rho_f H^{f_i}_f \frac{1}{\mu_f} \mathbf{K}^{f_i} \cdot \nabla p^{f_i}\right) - \nabla \cdot \left(\Lambda^{f_i}_{eff} \cdot \nabla T^{f_i}\right) =$$
$$= \rho_f H^{f_i}_f q^{f_i w} + \rho_f^* H_f^* \mathscr{Q}^{f_i m} + \sum_{j=1}^{n_{frac}}\left(\rho_f^* H_f^* \mathscr{Q}^{f_i f_j}\right)_{j \neq i} + \mathscr{R}^{f_i m} + \sum_{j=1}^{n_{frac}}\left(\mathscr{R}^{f_i f_j}\right)_{j \neq i},$$
$$\text{on} \quad \Omega_{f_i} \subseteq \text{Re}^{n-1} \quad \forall i \in \{1, ..., n_{frac}\}, \tag{9}$$

for the lower dimensional fracture (f_i). Here, the two main unknowns are pressure p and temperature T (in both fluid and solid rock). $(\rho U)_{eff}$ is the effective property defined as

$$(\rho U)_{eff} = \phi \rho_f U_f + (1 - \phi)\rho_r U_r, \tag{10}$$

where U_f and U_r are the specific internal energy in fluid and rock respectively. Distinctively, $(\rho U)^m_{eff} = \phi^m \rho_f U_f + (1 - \phi^m)\rho_r U_r$ and $(\rho U)^{f_i}_{eff} = \phi^{f_i}\rho_f U_f + (1 - \phi^{f_i})\rho_r U_r$. In addition, H_f is the specific fluid enthalpy. The three mentioned terms can be expressed as non-linear functions of pressure and temperature. Λ_{eff} is the effective thermal conductivity of the saturated rock written as

$$\Lambda_{eff} = \phi \Lambda_f + (1 - \phi)\Lambda_r. \tag{11}$$

Here, Λ_f and Λ_r are the thermal conductivities in fluid and rock, respectively. The subscripts f and r indicate fluid and solid rock. Note that, $\Lambda^m_{eff} = \phi^m \Lambda_f + (1 - \phi^m)\Lambda_r$ and $\Lambda^{f_i}_{eff} = \phi^{f_i}\Lambda_f + (1 - \phi^{f_i})\Lambda_r$. Lastly, $\mathscr{R}^{mf_i}$ and $\mathscr{R}^{f_im}$ are the conductive heat flux exchange between matrix m and the overlapping fracture f_i. $\mathscr{R}^{f_if_j}$ denotes the conductive heat flux exchange from j-th fracture to the i-th fracture where the intersection occurs. Similar to mass flux exchange, the conductive flux exchange terms are non-zero only for the existing matrix-fracture overlaps or fracture-fracture intersections. $\iiint_V \mathscr{R}^{mf_i} dV = - \iint_{A_{f_i}} \mathscr{R}^{f_im} dA$, and $\iint_{A_{f_i}} \mathscr{R}^{f_if_j} dA = - \iint_{A_{f_j}} \mathscr{Q}^{f_jf_i} dA$ hold as well to honor the conservation of energy.

To obtain the conductive heat flux exchanges, i.e., $\mathscr{R}^{mf_i}$, $\mathscr{R}^{f_im}$ (matrix-fracture connectivities) and $\mathscr{R}^{f_if_j}$ (fracture-fracture connectivities), the embedded discrete scheme is used, i.e.,

$$\mathscr{R}^{mf_i} = CI^{mf_i} \cdot \Lambda^*_{eff} \cdot (T^{f_i} - T^m) \tag{12}$$

$$\mathscr{R}^{mf_i} = CI^{f_im} \cdot \Lambda^*_{eff} \cdot (T^m - T^{f_i}) \tag{13}$$

$$\mathscr{R}^{f_if_j} = CI^{f_if_j} \cdot \Lambda^*_{eff} \cdot (T^{f_j} - T^{f_i}), \tag{14}$$

where Λ^*_{eff} is obtained as harmonically-averaged property between the two non-neighboring elements. CI is identical to the connectivity index used in Eq. (5).

Correlations

The following correlations are used to compute certain fluid and rock properties.

Fluid viscosity: Viscosity as a function of temperature is calculated via the following correlation (Al-Shemmeri, 2012),

$$\mu_f(T) = 2.414 \times 10^{-5} \times 10^{\frac{247.8}{T - 140}}.$$

Fluid density: The density of fluid is a function of pressure and temperature, defined as (Coats, 1977)

$$\rho_f(P,T) = \rho_{fs}(T)[1 + c_w(T)(P - P_s)],$$

where $P_S = 1\,\text{bar}$. $c_w(T)$ and $\rho_{fs}(T)$ are computed from the following empirical correlations (Praditia et al., 2018; Wagner and Kretzschmar, 2008)

$$c_w(T) = (0.0839\,T^2 + 652.73\,T - 203714) \times 10^{-12}$$

$$\rho_{fs}(T) = -0.0032\,T^2 + 1.7508\,T + 757.5.$$

**Fluid Entalphy:** Fluid enthalpy is obtained via (Coats, 1977)

$$H_f(P,T) = u_{ws} + C_{pf}(T - T_s) + \frac{P}{\rho_f},$$

where $u_{ws} = 420000\,\text{J/kg}$.

Corner-point Grid

A corner-point grid is defined with a set of straight pillars outlined by their endpoints over a Cartesian 2D mesh in the lateral direction (Lie, 2019). On every pillar, a constant number of nodes (corner-points) is set, and each cell in the grid is set between 4 neighbouring pillars and two neighbouring points on each pillar. Every cell can be identified by integer coordinates (i,j,k); where the k coordinate runs along the pillars, and i and j span each layer. The cells are ordered naturally with the i-index (x-axis) cycling fastest, then the j -index (y-axis), and finally the k-index (negative z-direction).

For establishing more accurately vertical and inclined faulting, it is advantageous to define the position of the grid cell by its corner point locations and displace them along the pillars that have been aligned with faults surfaces. Similarly, for modelling erosion surfaces and pinch-outs of geological layers, the corner point format allows points to collapse along coordinate lines. The corner points can collapse along all four lines of a pillar so that a cell completely disappears in the presence of erosion surfaces. If the collapse is in some pillars, the degenerate hexahedral cells may have less than six faces. This procedure creates non-matching geometries and non-neighbouring connections in the underlying i j k topology (Lie, 2019).
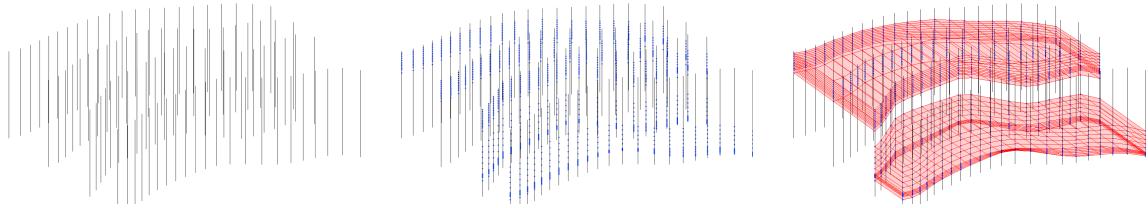
Figure 1: *Construction of a corner-point grid: Starting from the coordinate lines defining pillars (left), the corner-points are added to them (middle). A stack of cells is created for each set of four lines defining a pillar and at last the full grid is obtained.*

Two-Point Flux-Approximation

The linear elliptic equation serves a model pressure equation for incompressible fluids, i.e.,

$$\nabla \cdot u = f, \tag{15}$$

where f is the source/sink term (wells), and u is the Darcy velocity, defined as

$$u = -\mathbf{K}\nabla p. \tag{16}$$

Finite volume discrete systems can be obtained by rewriting the equation in integral form, on discrete cell Ω_i, as

$$\int_{\partial \Omega_i} \vec{u} \cdot \vec{n} \, dS = - \int_{\Omega_i} q \, d\vec{x}. \tag{17}$$

The flux between the two neighbouring cells i and k can be then written as

$$u_{i,k} = \int_{\Gamma_{i,k}} \vec{u} \cdot \vec{n} \, dS. \tag{18}$$

The faces $\Gamma_{i,k}$ are denominated half face as they are linked with a grid cell Ω_i and a normal vector $\vec{n}_{i,k}$. It is assumed that the grid is matching to another one so that each interior half face will have a twin half

face $\Gamma_{k,i}$ that also has an identical area $A_{i,k} = A_{k,i}$ but opposite normal vector $\vec{n}_{i,k} = -\vec{n}_{k,i}$. The integral over the cell face is approximated by the midpoint rule, and Darcy's law, i.e.,

$$u_{i,k} \approx A_{i,k} \left(\mathbf{K} \nabla p \right) \left(\vec{x}_{i,k} \right) \cdot \vec{n}_{i,k} \tag{19}$$

where $\vec{x}_{i,k}$ indicates the centroid of $\Gamma_{i,k}$.

The one-sided finite difference is used to determine the pressure gradient as the difference between the pressure $\pi_{i,k}$ at the face centroid and the pressure at some point inside the cell. The reconstructed pressure value at the cell centre is equal to the average pressure p_i inside the cell, thus,

$$u_{i,k} \approx A_{i,k} \mathbf{K_i} \frac{(p_i - \pi_{i,k})\vec{c}_{k,i}}{|\vec{c}_{k,i}|^2} \cdot \vec{n}_{i,k} \;\Rightarrow\; u_{i,k} \approx T_{i,k}(p_i - \pi_{i,k}). \tag{20}$$

The vectors $\vec{c}_{k,i}$ are defined from cell centroids to face centroids. Face normals are assumed to have a length equal to the corresponding face areas $A_{i,k} \cdot \vec{n}_{i,k}$, i.e.,

$$T_{i,k} = A_{i,k} \mathbf{K_i} \frac{\vec{c}_{k,i} \cdot \vec{n}_{i,k}}{|\vec{c}_{k,i}|^2} \tag{21}$$
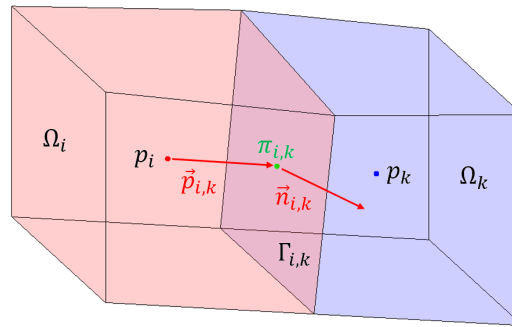
Figure 2: *Two cells used to define the two-point discretization on general polyhedral cells.*

The one-sided transmissibilities $T_{i,k}$ are related to a single cell and provide a two-point relation between the flux across a cell face and the pressure difference between the cell and face centroids. The proper name for these one-sided transmissibilities is half-transmissibilities as they are associated with a half face (Karimi-Fard et al., 2004; Bosma et al., 2017).

Finally, the continuity of fluxes across all faces, $u_{i,k} = -u_{k,i}$, as well as the continuity of face pressures $\pi_{i,k} = \pi_{k,i} = \pi_{ik}$ are set. This leads to

$$T_{i,k}^{-1} u_{ik} = p_i - \pi_{ik} \tag{22}$$

$$-T_{k,i}^{-1} u_{ik} = p_k - \pi_{ik}. \tag{23}$$

The interface pressure π_{ik} is then eliminated and the two-point flux approximation (TPFA) scheme is defined as

$$u_{ik} = \left[T_{i,k}^{-1} + T_{k,i}^{-1} \right]^{-1} (p_i - p_k) = T_{ik} (p_i - p_k). \tag{24}$$

T_{ik} is the transmissibility associated with the connection between the two cells. The TPFA scheme uses two "points", the cell averages p_i and p_k, to approximate the flux across the interface $\Gamma_{i,k}$ between cells

Ω_i and Ω_k. The TPFA scheme in a compact form obtains a set of cell averages that meet the following system of equations

$$\sum_k T_{ik} (p_i - p_k) = q_i, \quad \forall \Omega_i \subset \Omega. \tag{25}$$

Projection-based Embedded Discrete Fracture Model (pEDFM) for Corner-point Gird Geometry

As stated in the section of governing equations, sets of flux exchange terms are defined between matrix and explicit fractures. Inside each term, the connectivity index ($CI_{ij} = \frac{A_{ij}}{\langle d \rangle_{ij}}$) is considered. To calculate the area fraction (A_{ij}) of each overlapping fracture element inside the corresponding matrix grid cell, various geometrical functions are defined which can obtain the intersection between a tetragon (the 2D planar fracture grid cell in 3D geometry) and a hexahedron (the matrix grid cell in corner-point grid geometry). Once the intersection is obtained and the area fraction is calculated, the avergae distance ($\langle d \rangle_{ij}$) between the two overlapping elements is calculated as well. Figures 3 and 4 illustrate the geometry of CPG-based pEDFM grids. Note that the fractures can have any orientations in 3D, and arbitrary crossing lines with other fractures.

(a) matrix grid   *(b) fracture grids*
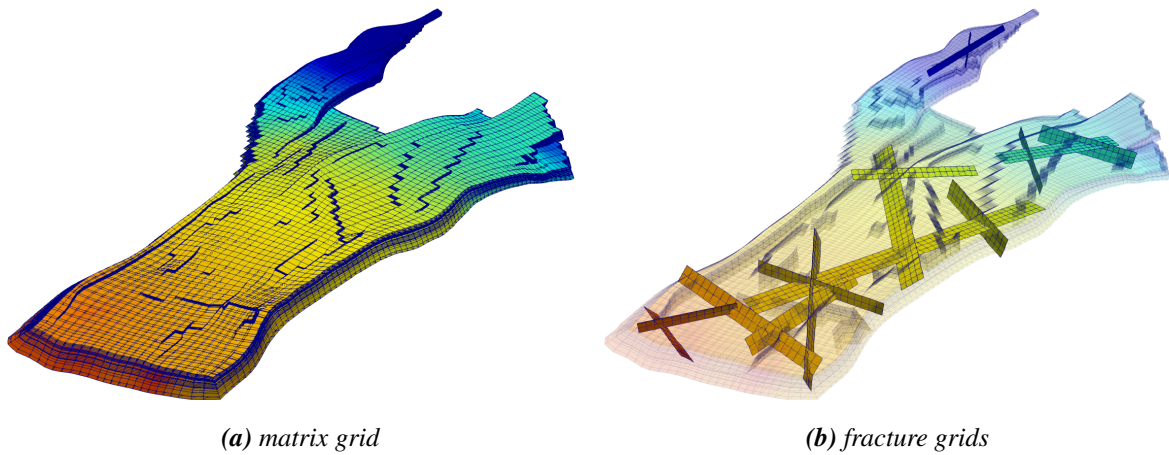
Figure 3: *An example of a fractured domain on corner-point grid geometry. The domain presented in the left image is the well-known Norne oil-field which is a true representative of the real-field geometry (Lie, 2019). The figure on the right is a realisation of a fracture network inside the domain that was exclusively designed by the authors of this paper. Note that each sub domain (matrix, and individual fractures) entail independent grid resolutions, and can have independent complexities (e.g. 3D orientation).*
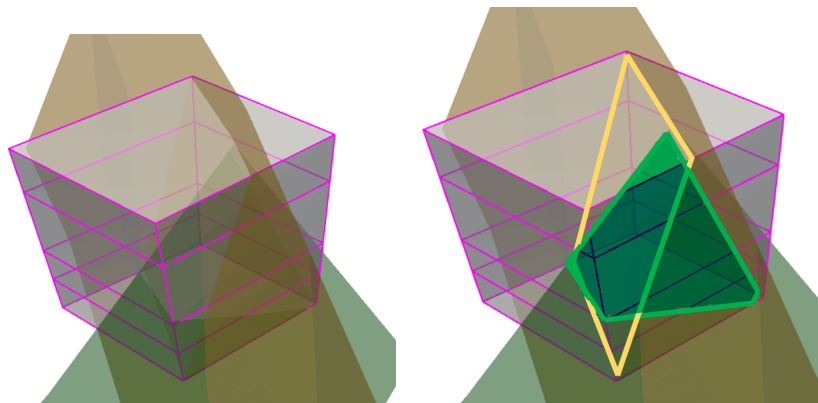
Figure 4: *The intersection between to fractures and a hexahedron from corner-point grid geometry is illustrated here. The figure on the right highlights the area fraction of the two separate fracture plates inside the matrix grid cell. The overlapping segment of green fracture forms an irregular pentagon where the orange fracture has a tetragon overlapping segment.*

To develop pEDFM for CPG geometries, first, all the connectivities between each two neighbouring

matrix cells that are disconnected due to the overlapping fractures are detected. Due to geometrical algorithm devised during the development of this method, a continuous projection path (visible in Fig. 5 as solid lines in light-blue colour) is automatically obtained on the interfaces. As such it disconnects the neighbouring connections letting the flux occur only on one consistent route (i.e., through matrix-fracture-matrix). Please note that despite the structured grid representation of pEDFM projections in this figure, the general corner-point grid is used in this method. However, structured grid is used for the sake of simplicity of the illustration.

Let fracture element f overlap matrix grid cell i (as shown in Fig. 5) with an area fraction of A_{if}. A set of projections is defined on the interface between the overlapped matrix grid cell i and its neighbouring grid cells (in orange) that are affected by the crossing (i.e., j and k). Please note that in the 3D dimensional case, there will be three projections. For each dimension (i.e., x, y and z) the projection area fractions are obtained via

$$A_{if\perp x_e} = A_{if} \times \cos(\gamma), \quad x_e \in \{x, y, z\}, \tag{26}$$

where γ is the angle between the fracture element and the interface connecting the matrix grid cell i and the neighbouring grid cell in the corresponding dimension on the zoomed-in section and highlighted in red color as $A_{if\perp x}$ and $A_{if\perp y}$). New transmissibilities are defined to connect the fracture element f to each non-neighboring matrix grid cells (i.e., j and k in the 2D example shown in Fig. 5):

$$T_{i_e f} = \frac{A_{if\perp x_e}}{\langle d \rangle_{i_e f}} \lambda_{i_e f}, \quad x_e \in \{x, y, z\}, \tag{27}$$

where, $\langle d \rangle_{i_e f}$ is the average distance between the fracture element f and matrix grid cell i_e. $\lambda_{i_e f}$ is the effective fluid mobility between these cells. As a result of the new transmissibilities, the connectivity between the matrix grid cell i and its corresponding neighboring cells is modified:

$$T_{ii_e} = \frac{A_{ii_e} - A_{if\perp x_e}}{\Delta x_e} \lambda_{i_e f}, \quad \mathfrak{X} \in \{x, y, z\}. \tag{28}$$

For simplicity of the implementation, the modified transmissiblities are obtained by multiplication of coefficient α as a fraction of the projected cross-section area, and the cross-section area of the corresponding interface. Please note that for all overlapping fracture elements (except for the boundaries of the fractures), the projection will cover the whole interface. Therefore, α is 1.0 for most of the cases, resulting in zero transmissibility between the matrix grid cells (i.e., $T_{ii_e} = 0$), thus removing the parallel transmissibilities (Tene et al., 2017).

Results

Numerical results of three test cases are presented in this section. The first two test cases compare the pEDFM model on Cartesian grid and corner-point grid geometry visually. The third test cases demonstrates the pEDFM result on a geologically relevant field using corner-point grid geometry.

Table 1 shows the input parameters that are used for all the test cases mutually.

Test Case 1: 2D Heterogeneous fractured reservoir (box)

In this test case, pEDFM on Cartesian grid versus corner-point grid geometry is visually compared. For this reason, a box-shaped heterogeneous $100\,\text{m} \times 100\,\text{m}$ domain containing 30 fractures with mixed conductivities is considered. The length of each fracture is different but the size of their aperture is
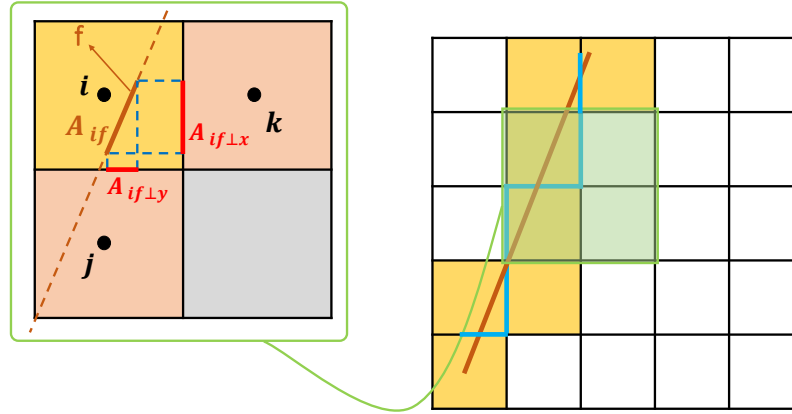
Figure 5: *pEDFM Illustration for a 2D matrix and a 1D overlapping fracture. The overlapped matrix cells are highlighted in yellow color. With classical EDFM method, these cells are connected to each overlapping fracture element via the connectivity index in the matrix-fracture flux exchange. pEDFM introduces extra non-neighboring connections between fracture elements and matrix cells highlighted in orange.*
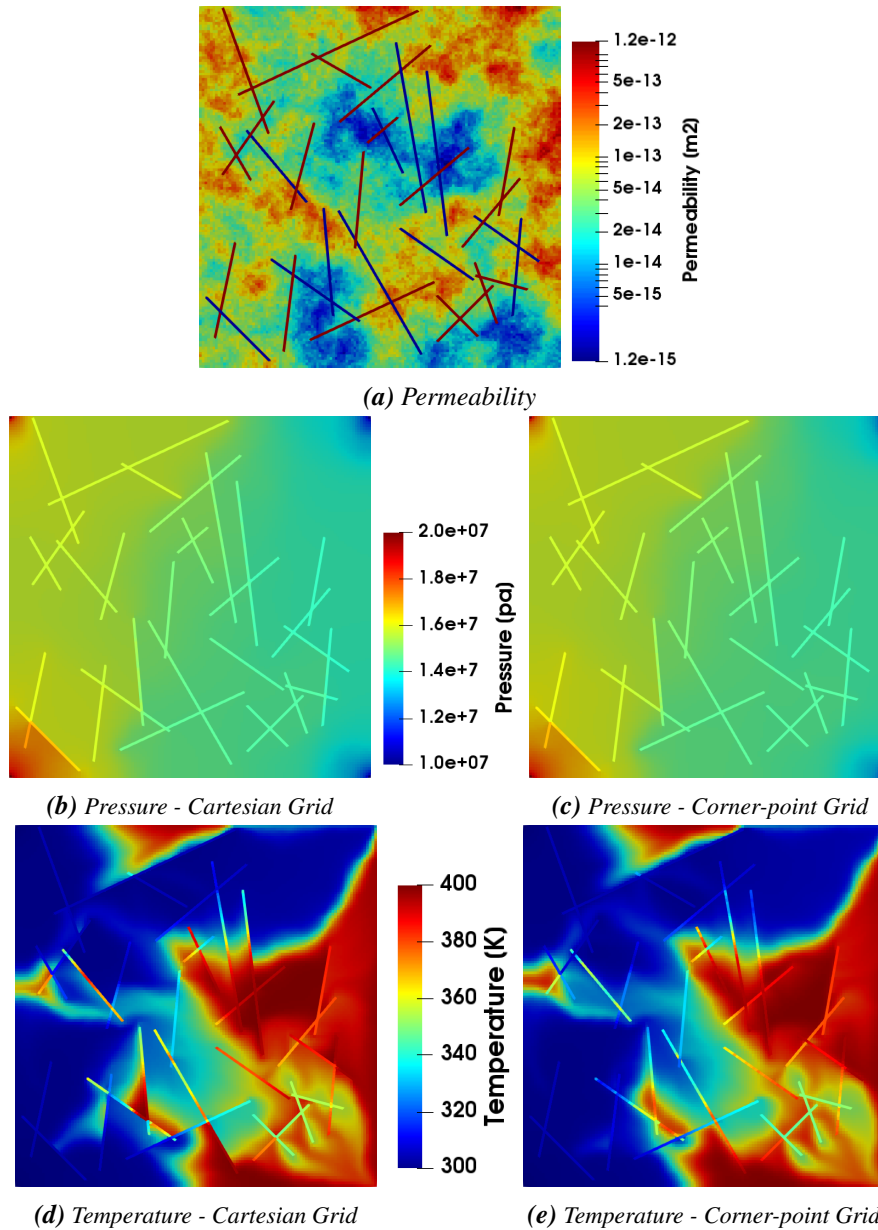
Table 1: *Input parameters of fluid and rock properties used in all test cases.*

Property	value
Rock thermal conductivity (Λ_r)	4 [W/m.K]
Fluid thermal conductivity (Λ_f)	0.591 [W/m.K]
Rock density (ρ_r)	2750 [kg/m^3]
Fluid specific heat (C_{p_f})	4200 [J/kg.K]
Rock specific heat (C_{p_r})	790 [J/kg.K]
Matrix porosity (ϕ)	0.2
fractures permeability (min)	10^{-20} [m^2]
fractures permeability (max)	10^{-8} [m^2]
Fractures aperture	5×10^{-3} [m]
Initial pressure of the reservoir	2×10^7 [Pa]
Initial temperature of the reservoir	400 [K]
Injection Pressure	5×10^7 [Pa]
Injection Temperature	300 [K]
Production Pressure	1×10^7 [Pa]

identical and set to $a_f = 5 \cdot 10^{-3}$ m. A 136×136 grid is imposed on the rock matrix and the fracture network consists of 1024 grid cells (in total 19520 cells). The permeability of the matrix ranges from $K_{m_{min}} = 1.2 \times 10^{-15}$ m^2 to $K_{m_{max}} = 1.2 \times 10^{-12}$ m^2. and the permeability of the fracture network has the range of $K_{f_{min}} = 10^{-20}$ m^2 and $K_{f_{max}} = 10^{-8}$ m^2. Two injection wells are located at the bottom left and top left corners with injection pressure of $p_{\text{inj}} = 2 \cdot 10^7$ Pa. additionally, there are two production wells at the bottom right and the top right corners with pressure of $p_{\text{prod}} = 1 \cdot 10^7$ Pa. Table 1 demonstrates the input parameters of this test case. Figure 6 shows the results of the simulation using both Cartesian Grid and corner-point geometry.

Test Case 2: 3D Heterogeneous fractured reservoir (box)

This test cases, similar to the test case 1, shows a visual comparison for pEDFM on Cartesian gird versus corner-point grid geometry. A 3D $100\,\text{m} \times 100\,\text{m} \times 40\,\text{m}$ domain containing 15 lower dimensional fractures with different geometrical properties is considered. An $50 \times 50 \times 20$ grid is imposed on rock matrix. The fracture network contains 1414 grid cells (total of 51414 grid cells). The rock matrix has permeability of $K_m = 10^{-14}$ m^2. Fracture network consists of both highly conductive fractures with

(a) Permeability

(b) Pressure - Cartesian Grid

(c) Pressure - Corner-point Grid

(d) Temperature - Cartesian Grid

(e) Temperature - Corner-point Grid

Figure 6: *Test case 1: 2D Heterogeneous. Fig. 6a illustrates the permeability map of the system. The figures 6b and 6c show the pressure solution on a specific time-step for Cartesian grid and corner-point grid geometry respectively. The figures on the bottom row (6d and 6e) visualize the temperature solutions on the same time-step.*

permeability of $K_f = 10^{-8} \, \text{m}^2$ and flow barriers with permeability of $K_f = 10^{-20} \, \text{m}^2$. Two injection wells exist on the bottom left and top left boundaries with pressure of $p_{\text{inj}} = 5 \cdot 10^7 \, \text{Pa}$. Similarly, two production wells are located at the bottom right and top right boundaries with pressure of $p_{\text{prod}} = 1 \cdot 10^7 \, \text{Pa}$. All wells are vertical and perforate the entire thickness of the reservoir. Figure 7 illustrates the results of the simulation using both Cartesian Grid and corner-point geometry.

(a) Pressure - Cartesian Grid   *(b) Pressure - Corner-point Grid*

(c) Temperature - Cartesian Grid   *(d) Temperature - Corner-point Grid*
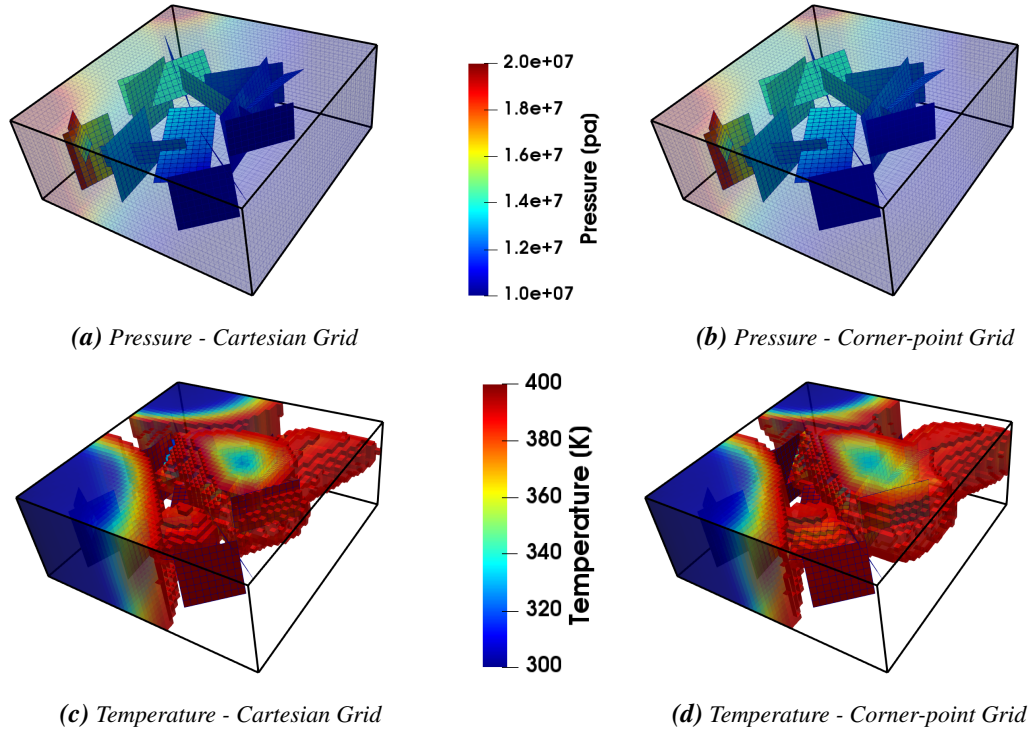
Figure 7: *Test case 2: 3D Homogeneous. The figures 7a and 7b show the pressure solution on a specific time-step for Cartesian grid and corner-point grid geometry respectively. The figures on the bottom row (7c and 7d) visualize the temperature solutions on the same time-step.*

Test Case 3: Norne oil-field with highly conductive fractures

This test case demonstrates the capability of pEDFM model on geologically relevant discrete system using corner-point grid geometry. The CPG data was extracted from the input files of MATLAB Reservoir Simulation Toolbox (MRST) (Lie, 2019).

Norne is an oil field located around 80 kilometers north of the Heidrun oil field in the Norwegian Sea (Lie, 2019). As described in the MRST (Lie, 2019), the extent of this oil field is $10 \, \text{Km} \times 2 \, \text{Km} \times 100 \, \text{m}$. The corner-point grid skeleton consists of $46 \times 112 \times 22$ grid cells from which 44915 grid cells are active forming the complex geometrical shape of this oil field (Fig. 3). A network of 15 fractures (designed by the author as a realization) is considered inside this domain. The permeability of the Norne rock matrix in this test case is assumed to be constant at $K_m = 10^{-14} \, \text{m}^2$. All fractures are highly conductive with permeability of $K_f = 10^{-8} \, \text{m}^2$. Two injection wells with pressure of $p_{\text{inj}} = 5 \cdot 10^7 \, \text{Pa}$ and two production wells with pressure of $p_{\text{prod}} = 1 \cdot 10^7 \, \text{Pa}$ are located in the outer skirts of the reservoir as it can be seen on Fig. 8a. All wells are vertical and perforate the entire thickness of the reservoir.

Conclusions

A projection-based embedded discrete fracture model (pEDFM) for corner-point grid (CPG) geometry was developed and presented for fully-implicit simulation of single-phase coupled mass-heat flow in fractured heterogeneous porous media. First, the pEDFM model Tene et al. (2017); HosseiniMehr et al. (2020b) is extended to account for fully 3D fracture geometries on generic corner-point grid discrete system. Through a number of homogeneous and heterogeneous test cases, the performance of pEDFM

(a) Pressure - Matrix

(b) Pressure - Fractures

(c) Temperature - Cartesian Grid
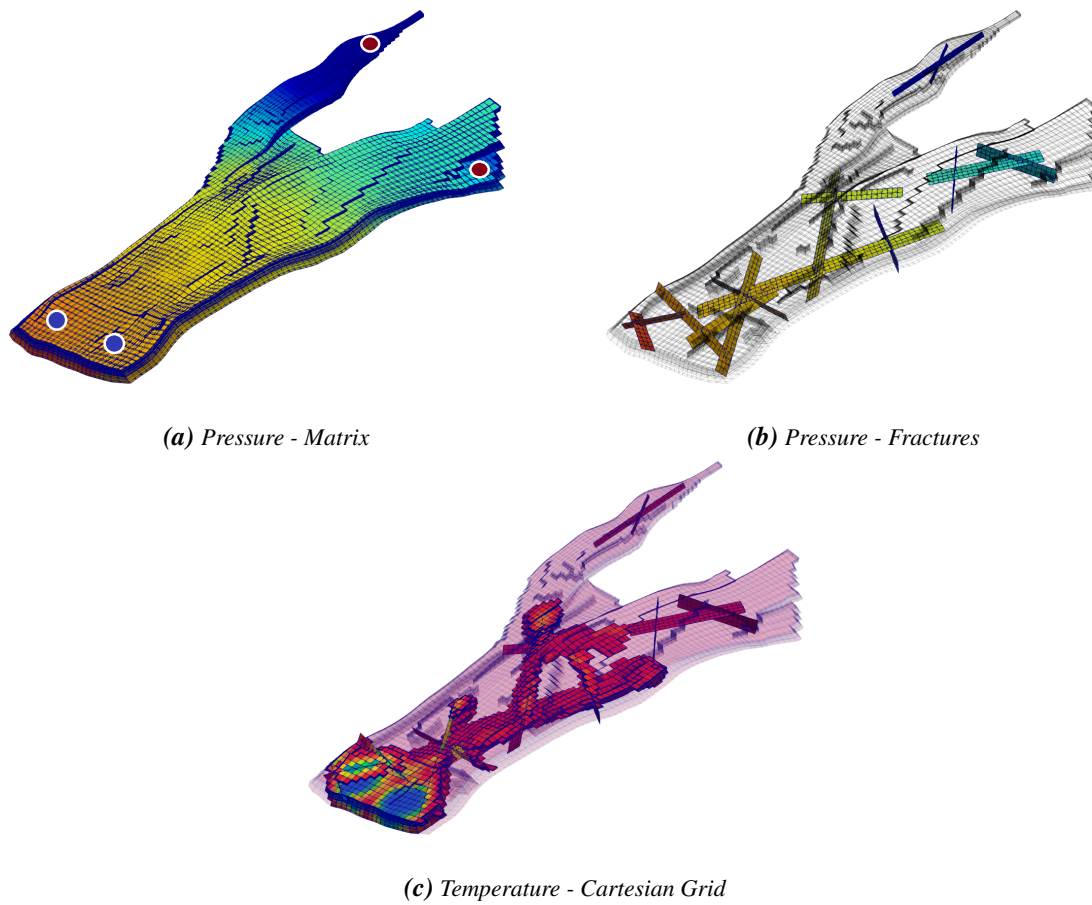
Figure 8: *Test case 3: Norne oil field. The figures 8a and 8b show the pressure solutions of the matrix and the embedded fractures. The figure on the bottom row (8c) visualizes the temperature solution on the same time-step.*

on CPG was briefly demonstrated.

Moreover, numerical results are obtained for 2D and 3D geothermal reservoirs. These fine-scale simulation for a 2D and 3D geothermal system allows for both highly conductive and flow-barrier fractures. It is shown that pEDFM can accurately capture the physical influence of both highly conductive fractures and flow barriers on the flow patterns.

All software developments of this work is made available open source at https://gitlab.com/DARSim2simulator.

Acknowledgments

Authors would like to thank all the members of the Delft Advanced Reservoir Simulation (DARSim) research team for the fruitful discussions during the development of this method.

References

Ahmed, R., Edwards, M.G., Lamine, S., Huisman, B.A.H. and Pal, M. [2015] Control-volume distributed multi-point flux approximation coupled with a lower-dimensional fracture model. *J. Comput. Phys.*, **284**, 462–489.

Al-Shemmeri, T.T. [2012] Engineering Fluid Mechanics. chap. 1, Bookboon, 18.

Berkowitz, B. [2002] Characterizing flow and transport in fractured geological media: A review. *Advances in water resources*, **25**(8-12), 861–884.

Bertani, R. [2012] Geothermal power generation in the world 2005-2010 update report. *Geothermics*, **41**, 1–29.

Bosma, S.B.M., Hajibeygi, H., Tene, M., Tchelepi, H.A. and Others [2017] Multiscale Finite Volume Method for Discrete Fracture Modeling with Unstructured Grids. *SPE Reservoir Simulation Conference*, **351**, 145–164.

Burnell, J., Clearwater, E., A., C., Kissling, W., OSullivan, J., OSullivan, M. and Yeh, A. [2012] Future directions in geothermal modelling. In: *In Proceedings (electronic) 34rd New Zealand Geothermal Workshop*. 19–21.

Burnell, J., OSullivan, M., OSullivan, J., Kissling, W., Croucher, A., Pogacnik, J., Pearson, S., Caldwell, G., Ellis, S., Zarrouk, S. and Climo, M. [2015] Geothermal supermodels: the next generation of integrated geophysical, chemical and flow simulation modelling tools. In: *In Proceedings World Geothermal Congress*. 19–21.

Coats, K.H. [1977] Geothermal Reservoir Modelling. In: *SPE Annual Fall Technical Conference and Exhibition*.

Cusini, M., Fryer, B., van Kruijsdijk, C. and Hajibeygi, H. [2018] Algebraic dynamic multilevel method for compositional flow in heterogeneous porous media. *J. Comput. Phys.*, **354**, 593–612.

Ding, Y., Lemonnier, P. and Others [1995] Use of corner point geometry in reservoir simulation. In: *International Meeting on Petroleum Engineering*. Society of Petroleum Engineers.

Gan, Q. and Elsworth, D. [2016] Production optimization in fractured geothermal reservoirs by coupled discrete fracture network modeling. *Geothermics*, **62**, 131–142.

Garipov, T.T., Karimi-Fard, M. and Tchelepi, H.A. [2016] Discrete fracture model for coupled flow and geomechanics. *Computational Geosciences*, **20**(1), 149–160.

GeoQuest, S. [2014] ECLIPSE reference manual. *Schlumberger, Houston, Texas*.

Gholizadeh Doonechaly, N., Abdel Azim, R. and Rahman, S.S. [2016a] Evaluation of recoverable energy potential from enhanced geothermal systems: a sensitivity analysis in a poro-thermo-elastic framework. *Geofluids*, **16**(3), 384–395.

Gholizadeh Doonechaly, N., Abdel Azim, R.R. and Rahman, S.S. [2016b] A study of permeability changes due to cold fluid circulation in fractured geothermal reservoirs. *Groundwater*, **54**(3), 325–335.

Hajibeygi, H., Karvounis, D. and Jenny, P. [2011] A hierarchical fracture model for the iterative multiscale finite volume method. *Journal of Computational Physics*, **230**(24), 8729–8743.

HosseiniMehr, M., Vuik, C. and Hajibeygi, H. [2020a] Adaptive Dynamic Multilevel Simulation of Fractured Geothermal Reservoirs. *Journal of Computational Physics: X*, 100061.

HosseiniMehr, M., Vuik, C. and Hajibeygi, H. [2020b] Adaptive Dynamic Multilevel Simulation of Fractured Geothermal Reservoirs. *Journal of Computational Physics: X*, 100061.

Jiang, J. and Younis, R.M. [2016] Hybrid Coupled Discrete-Fracture/Matrix and Multicontinuum Models for Unconventional-Reservoir Simulation. *SPE Journal*, **21**(03), 1009–1027.

Jiang, J. and Younis, R.M. [2017] An improved projection-based embedded discrete fracture model (pEDFM) for multiphase flow in fractured reservoirs. *Advances in Water Resources*, **109**, 267 – 289.

Karimi-Fard, Durlofsky, L.J. and K.Aziz [2004] An Efficient Discrete-Fracture Model Applicable for General-Purpose Reservoir Simulators. *SPE Journal*, 227–236.

Kozlova, A., Li, Z., Natvig, J.R., Watanabe, S., Zhou, Y., Bratvedt, K., Lee, S.H. and Others [2016] A real-field multiscale black-oil reservoir simulator. *SPE Journal*.

Leal, A.M.M., Kulik, D.A., Smith, W.R. and Saar, M.O. [2017] An overview of computational methods for chemical equilibrium and kinetic calculations for geochemical and reactive transport modeling. *Pure and Applied Chemistry*, **89**(5), 597–643.

Lee, S.H., Jensen, C.L. and Lough, M.F. [1999] An Efficient Finite Difference Model For Flow In a Reservoir With Multiple Length-Scale Fractures. *SPE ATCE*.

Lee, S.H., Lough, M.F. and Jensen, C.L. [2001] Hierarchical modeling of flow in naturally fractured formations with multiple length scales. *Water Resource Research*, **37**(3), 443–455.

Li, L. and Lee, S.H. [2008] Efficient field-scale simulation of black oil in naturally fractured reservoir through discrete fracture networks and homogenized media. *SPE Reservoir Evaluation and Engineering*, 750–758.

Lie, K.A. [2019] *An introduction to reservoir simulation using MATLAB/GNU Octave: User guide for the MATLAB Reservoir Simulation Toolbox (MRST)*. Cambridge University Press.

Lie, K.A., Mykkeltvedt, T.S. and Møyner, O. [2020] A fully implicit WENO scheme on stratigraphic and unstructured polyhedral grids. *Computational Geosciences*, **24**(2), 405–423.

Lund, J.W., Freeston, D.H. and Boyd, T.L. [2011] Direct utilization of geothermal energy 2010 worldwide review. *Geothermics*, **40**(3), 159–180.

McClure, M.W. and Horne, R.N. [2014] An investigation of stimulation mechanisms in Enhanced Geothermal Systems. *International Journal of Rock Mechanics and Mining Sciences*, **72**, 242–260.

Moinfar, A., Narr, W., Hui, M.H., Mallison, B.T., Lee, S.H. and Others [2011] Comparison of discrete-fracture and dual-permeability models for multiphase flow in naturally fractured reservoirs. In: *SPE reservoir simulation symposium*. Society of Petroleum Engineers.

Moraes, R.J.D., Rodrigues, J.R.P., Hajibeygi, H. and Jansen, J.D. [2017] Multiscale gradient computation for flow in heterogeneous porous media. *J. Comp. Phys.*, **336**(6), 644–663.

Morel, F. and Morgan, J. [1972] Numerical method for computing equilibriums in aqueous chemical systems. *Environmental Science & Technology*, **6**(1), 58–67.

Ponting, D.K. [1989] Corner point geometry in reservoir simulation. In: *ECMOR I-1st European Conference on the Mathematics of Oil Recovery*. European Association of Geoscientists & Engineers, cp—-234.

Praditia, T., Helmig, R. and Hajibeygi, H. [2018] Multiscale formulation for couple. *Computat. Geo.*, **(in press)**, DOI: 10.1007/s10596–018–9754–4.

Reichenberger, V., Jakobs, H., Bastian, P. and Helmig, R. [2006] A mixed-dimensional finite volume method for two-phase flow in fractured porous media. *Advances in Water Resources*, **29**, 1020–1036.

Ren, G., Jiang, J. and Younis, R.M. [2018] A Model for coupled geomechanics and multiphase flow in fractured porous media using embedded meshes. *Advances in Water Resources*, **122**, 113 – 130.

Rossi, E., Kant, M.A., Madonna, C., Saar, M.O. and von Rohr, P.R. [2018] The Effects of High Heating Rate and High Temperature on the Rock Strength: Feasibility Study of a Thermally Assisted Drilling Method. *Rock Mechanics and Rock Engineering*.

Salimzadeh, S., Grandahl, M., Medetbekova, M. and Nick, H.M. [2019] A novel radial jet drilling stimulation technique for enhancing heat recovery from fractured geothermal reservoirs. *Renewable energy*, **139**, 395–409.

Salimzadeh, S. and Nick, H.M. [2019] A coupled model for reactive flow through deformable fractures in Enhanced Geothermal Systems. *Geothermics*, **81**, 88–100.

Tene, M., Bosma, S.B.M., Kobaisi, M.S.A. and Hajibeygi, H. [2017] Projection-based Embedded Discrete Fracture Model (pEDFM). *Advances in Water Resources*, **105**, 205–216.

Voskov, D.V. [2017] Operator-based linearization approach for modeling of multiphase multi-

component flow in porous media. *Journal of Computational Physics*, **337**, 275 – 288.

Voskov, D.V. and Tchelepi, H.A. [2012] Comparison of nonlinear formulations for two-phase multi-component EoS based simulation. *J. Pet. Sc.*, **82-83**, 101–111.

Wagner, W. and Kretzschmar, H. [2008] *International Steam Tables - Properties of Water and Steam based on the Industrial Formulation IAPWS-IF97*. Springer, second edn.

Wang, Y., Voskov, D., Khait, M. and Bruhn, D. [2020] An efficient numerical simulator for geothermal simulation: A benchmark study. *Applied Energy*, **264**, 114693.

Wong, Z.Y., Horne, R.N. and Tchelepi, H.A. [2018] Sequential implicit nonlinear solver for geothermal simulation. *Journal of Computational Physics*, **368**, 236–253.

Xu, Y., Sepehrnoori, K. and Others [2019] Development of an Embedded Discrete Fracture Model for Field-Scale Reservoir Simulation With Complex Corner-Point Grids. *SPE Journal*, **24**(04), 1–552.